Supplementary Information : Tailoring Second Harmonic Generation in single L-shaped plasmonic nanoantennas from the capacitive to conductive coupling regime

Leo-Jay Black,[†,§] Peter R. Wiecha,[‡,§] Yudong Wang,[†] C. H. de Groot,[¶] Vincent Paillard,[‡] Christian Girard,[‡] Otto L. Muskens,[∗,†] and Arnaud Arbouet[∗,‡]

Physics and Astronomy, Faculty of Physical Sciences and Engineering, University of Southampton, Highfield, Southampton SO17 1BJ, United Kingdom, CEMES, UPR 8011,CNRS-Université de Toulouse, 29 Rue Jeanne Marvig, BP 94347, F-31055 Toulouse, France, and Nano Group, Faculty of Physical Sciences and Engineering, University of Southampton, Highfield, Southampton SO17 1BJ, United Kingdom

E-mail: O.Muskens@soton.ac.uk; arbouet@cemes.fr

[∗]To whom correspondence should be addressed

[†]Physics and Astronomy, Faculty of Physical Sciences and Engineering, University of Southampton, Highfield, Southampton SO17 1BJ, United Kingdom

[‡]CEMES, UPR 8011,CNRS-Université de Toulouse, 29 Rue Jeanne Marvig, BP 94347, F-31055 Toulouse, France

[¶]Nano Group, Faculty of Physical Sciences and Engineering, University of Southampton, Highfield, Southampton SO17 1BJ, United Kingdom

[§]Authors contributed equally

1 S1 - Linear optical properties of L-shaped nanoantennas
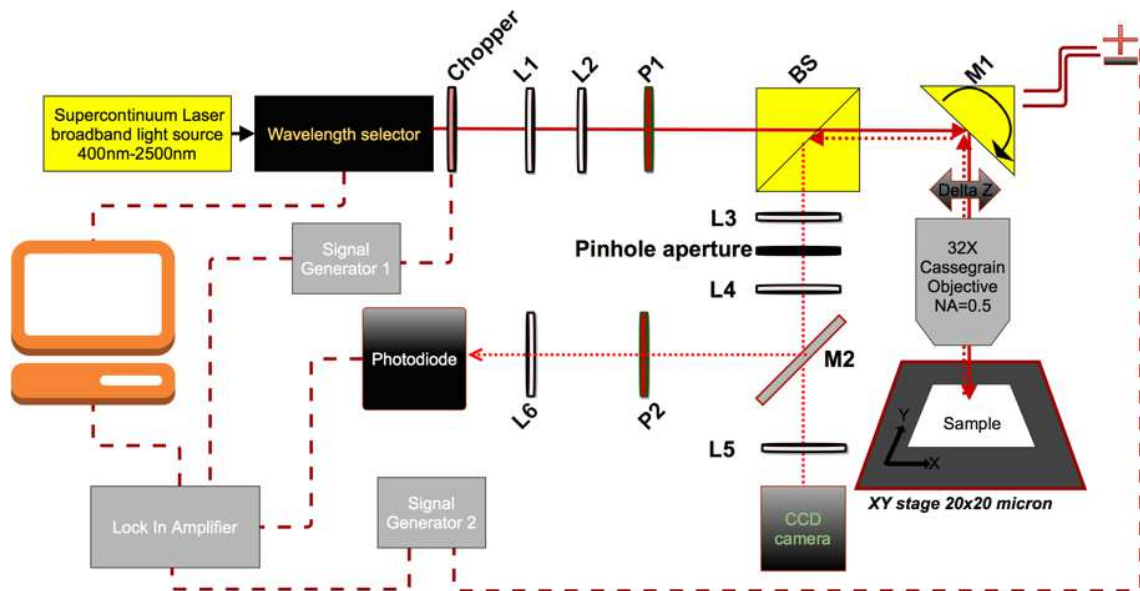
1.1 Spatial Modulation Spectroscopy

Figure S1: (color online) Experimental spatial modulation spectroscopy (SMS) setup. Polarizer 1 (P1) sets the polarization of the incident light, polarizer 2 (P2) is used for analysis of the scattered light. Mirror M1 is modulated using a piezo actuator. Mirror M2 is removable which allows imaging and positioning the antenna array. The pinhole aperture acts as a confocal spatial filter.

1.2 Extinction spectra of representative antennas

The linear optical properties of all the antennas investigated in this work have systematically been characterized using Spatial Modulation Spectroscopy (SMS). Figure S1 shows the experimental set-up in details. Figure S2a shows the extinction cross-section measured on three antennas representative of the three distinct situations that can be found in our samples : conductive coupling, capacitive coupling with small or large gaps. As can be noted on Figure S2a, the wavelength of the antibonding mode does not change much with the gap. On the contrary, the latter has a strong influence on the bonding mode. By comparing the

first two cases, it can be seen that for a fixed arm length, a decrease in gap width yields an increase in spectral splitting between the two eigenmodes. The third case of a fused antenna sees even larger splitting. Figure S2b shows the corresponding results of electrodynamical simulations which are in good agreement with the experiment.[1]
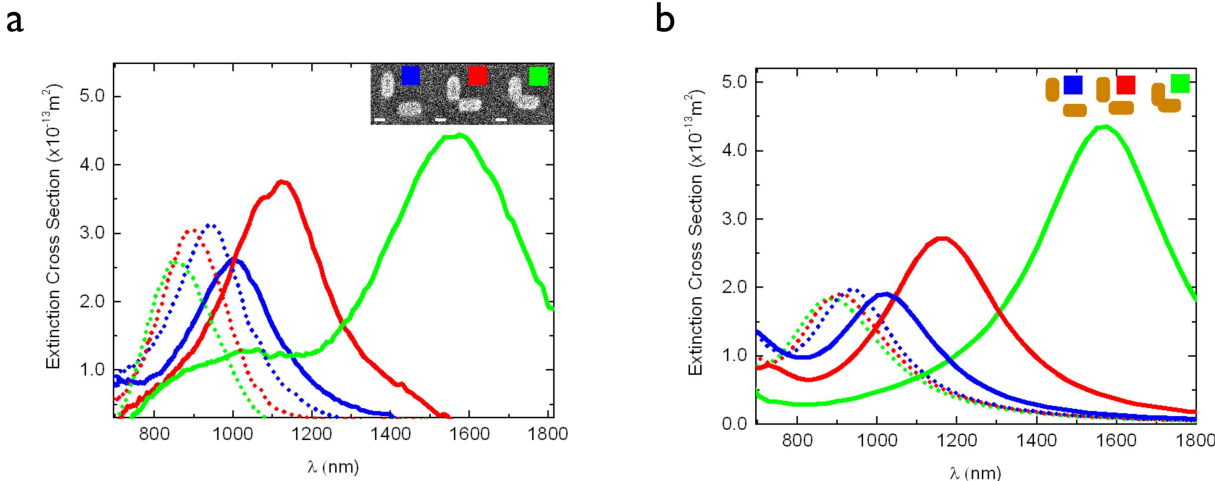

Figure S2: (color online) a) Extinction cross-section of three representative antennas measured using Spatial Modulation Spectroscopy (the corresponding SEM image is given in inset). The dashed (resp. solid) lines correspond to an incident polarization at 45° (resp. at −45°) i.e corresponding to the antibonding (resp. bonding) configuration. b) Corresponding computed extinction cross-sections.

1.3 Calculated near-field maps and spectral resonance positions of bonding and anti-bonding modes

Maps of the absolute near-field enhancement around the antennas are shown in Figure S3 for cases of resonant excitation of the anti-bonding and bonding modes. Similar to the experiments, the pump wavelength was fixed at 900 nm, while the length of the structures was selected to match the resonance conditions. Whereas the A-mode shows a node in field strength at the center of the gap, a strong near-field enhancement is obtained in case of the B-mode, due to the opposite induced charges at both sides of the gap.

Figure S4 shows calculated absorption cross-sections of the L-shaped nanoantennas for incident light polarized along 45° (a) and -45° (b), respectively corresponding to excitation of
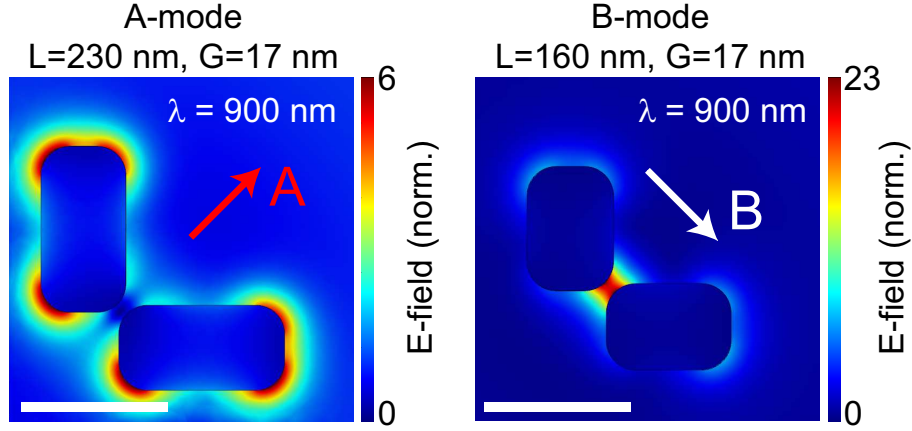
Figure S3: (color online) Near-field maps of electric field amplitude normalized to incident field, for anti-bonding (A) and bonding (B) modes.

the anti-bonding (A) and bonding (B) modes. Whereas the anti-bonding wavelength shows only a weak dependence on gap width, the bonding mode shows the pronounced scaling with gap, corresponding to a redshift for small capacitive gaps and a much larger renormalization of the spectrum for conductively coupled arms.[1] The dashed lines are guides to the eye representing the estimated peak position of the resonances A and B taken from these maps, which were used in the other graphs in this work to estimate the scaling of the SHG with the two corresponding resonance conditions.
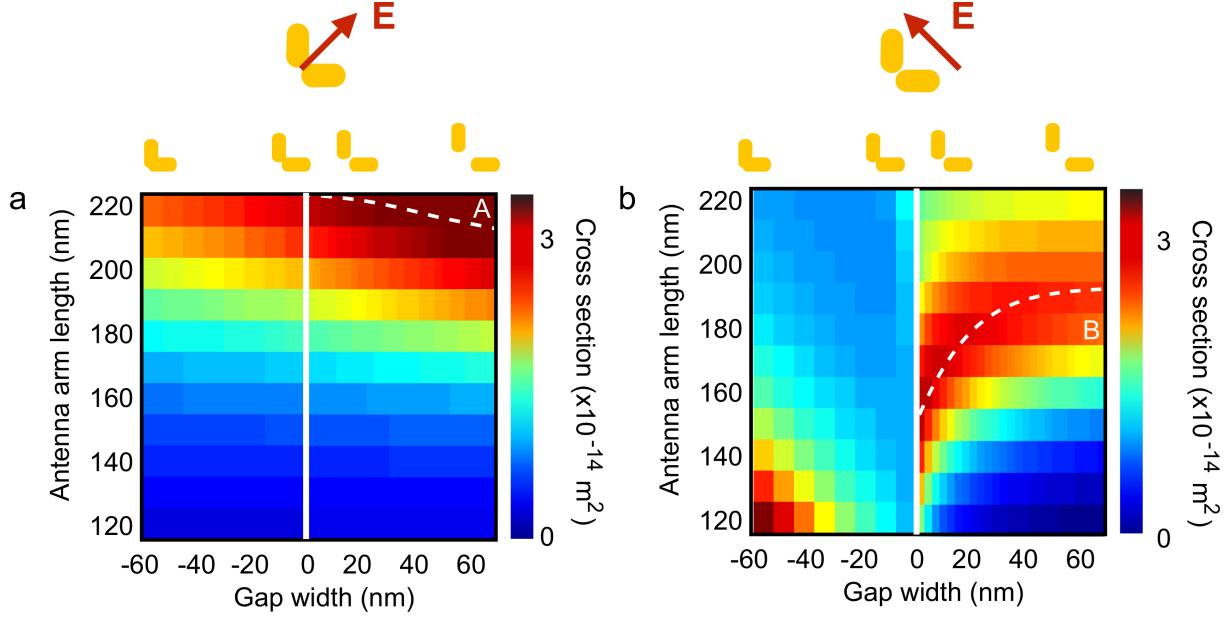
Figure S4: (color online) Map of antenna absorption cross section at $\lambda_{exc} = 900$ nm, as a function of antenna length L and gap width G. Dashed lines are guides to the eye indicating spectral positions of anti-bonding (A) and bonding (B) resonances.

2 S2 - Non-linear microscopy

2.1 Experimental set-up

Figure S5 shows the experimental setup. SHG is measured using a photomultiplier operating in photocurrent mode. After proper shielding of the detection box, the photocurrent noise level was 0.02 nA. In the Antibonding configuration, the detected photocurrent on the antennas (Figure 2a of the main text) goes from a maximum of 3.7 nA down to 0.2 nA for fused antennas and the noise level for only one disconnected antenna. In the Bonding configuration, the maximum photocurrent is 5.8 nA and the minimum is 0.08 nA. The relative uncertainty on the ratio $r = I_A/I_B$ between the SHG detected for an excitation along A and excitation along B is the sum of the relative uncertainties on the SHG intensities I_A and I_B. From the above values, we have checked that only for only one antenna the relative uncertainty on the calculated ratio is close to 0.5, the others having a much better precision.

Figure S6 shows the dependence of the detected signal with the excitation power. As
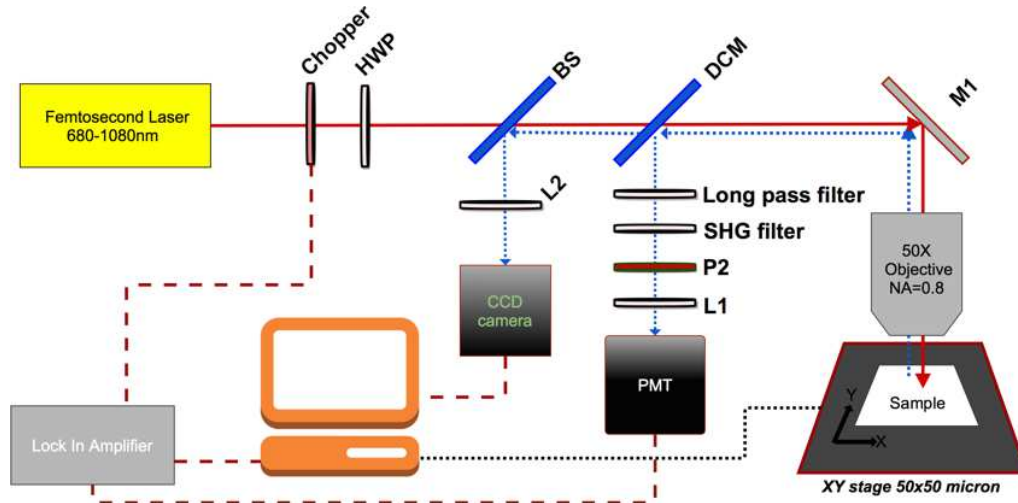
Figure S5: (color online) SHG measurement setup: the half wave plate (HWP) sets the incident polarisation, the dichroic mirror (DCM) reflects wavelengths smaller than the excitation wavelength, a photomultiplier (PMT) in photocurrent mode is used for SHG detection. Optional : polarizer 2 (P2) is used for analysis of the SHG light.

expected for a second order nonlinear process such as SHG, the nonlinear emission shows a quadratic dependence (slope ≈ 1.93).
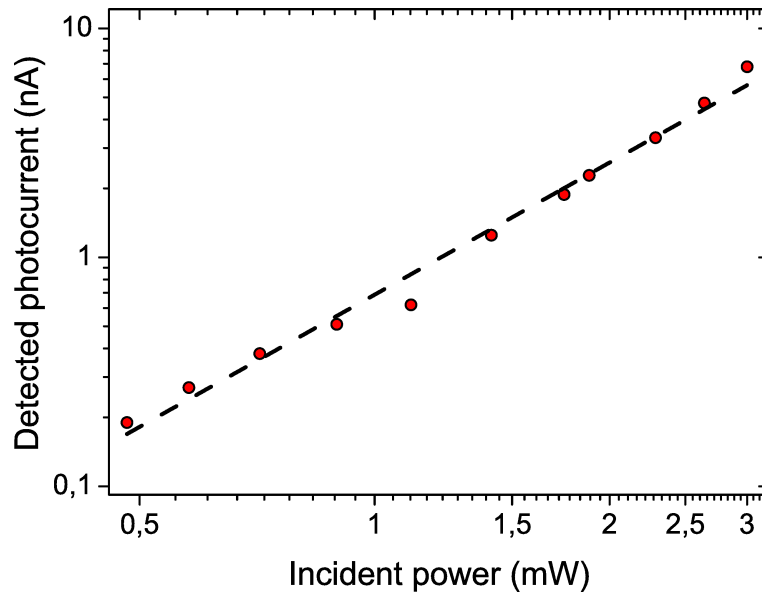

Figure S6: (color online) Detected nonlinear emission at different excitation powers (red dots). Assuming a power-law dependence, the numerical fit yields a value of 1.93 (dashed line).

2.2 SHG intensity maps

Figures S7a-c show the total detected SHG in the same configurations as Figure 2 of the main paper but measured on a different array. Within the limits of reproducibility achievable by EBL, the results are in good agreement with the ones presented in Figure 2 of the main text and with the results of the numerical simulations shown in Figure S7d-f. These numerical simulations have been performed under the same assumptions as in the main text, namely that the $\chi^{(2)}_{nnn}$ component of the nonlinear susceptibility tensor yields the largest contribution to SHG. This assumption and the influence of other components is discussed in the last part of this supplementary material. The difference between theory and experiment pointed out in the case of sub-20 nm disconnected gaps is also present in this array.

Figure S8 (resp. Figure S9) shows polarization-resolved SHG measurements performed on the same array as in Figure S7 for an excitation at 45° (resp. at −45°) together with the corresponding simulations. Compared to Figure 4 of the main paper in which both A and B contributions were simultaneously excited, the maps in Figure S8 and Figure S9 only show the contribution from one of the two eigenmodes supported by the antennas. Figure S8 and Figure S9 show that the polarization-resolved SHG intensity is generally in good agreement with the results of the microscopic model. As is discussed in the last part, the influence of other components of the nonlinear susceptibility tensor cannot explain the small differences observed in the SHG emission ratio (Fig. S9c and e).

In the bottom left corner of Figure S9a and Figure S9d, strong SHG from low aspect ratio antennas is detected. These objects, which resemble single nanorod oriented at -45° yield a stronger SHG along the B direction. This is illustrated in Figure S10 on the case of antenna denoted "A5" of Figure 1.
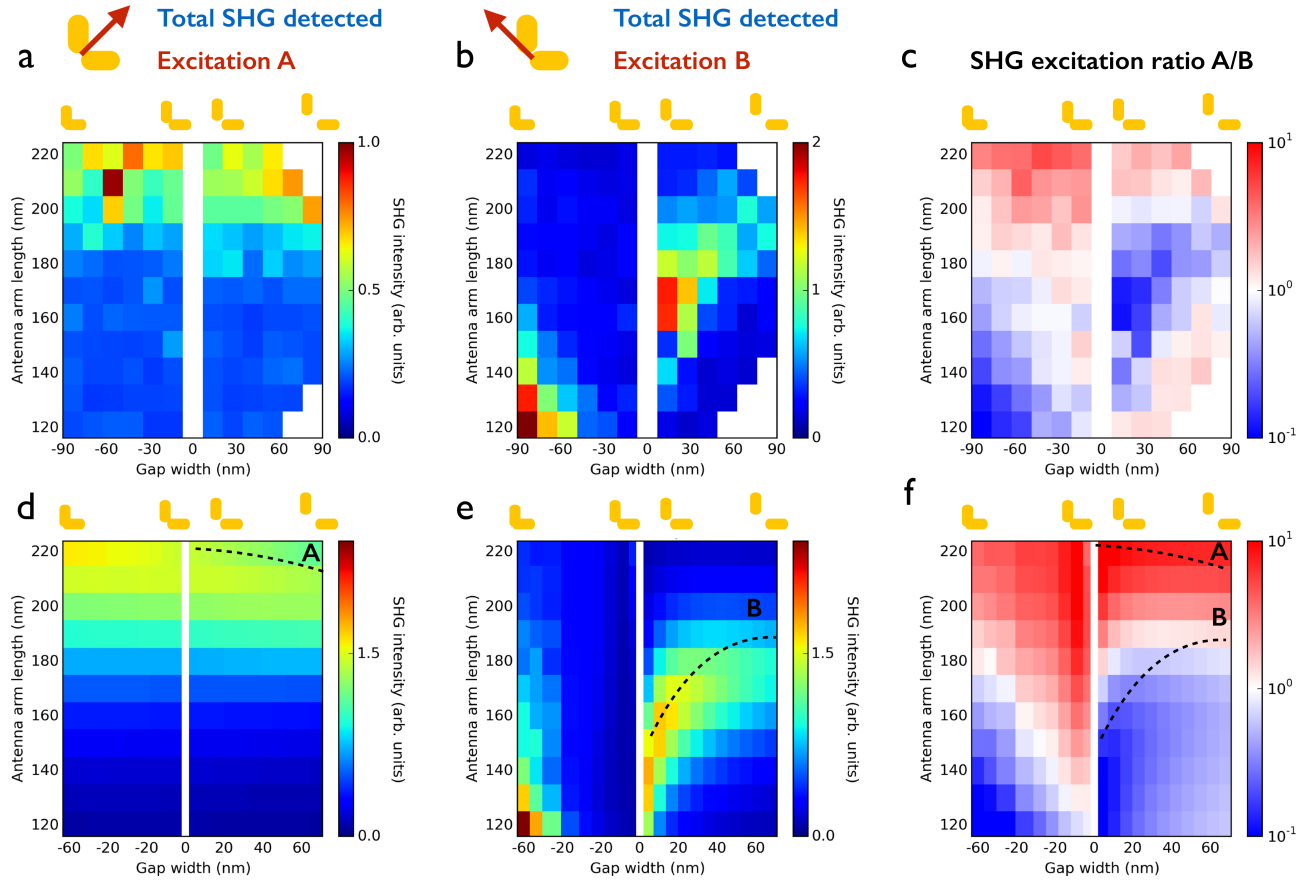
Figure S7: (color online) Total detected SHG for an incident E-field at 900 nm and linearly polarized along the anti-bonding (A) polarization of 45° (a) and bonding (B) polarization of -45° (b). c) Ratio of A/B excitation efficiencies obtained from a and b. d,e) Calculated excitation efficiency corresponding to geometries of a and b, with f) calculated ratio of A/B excitation efficiencies.
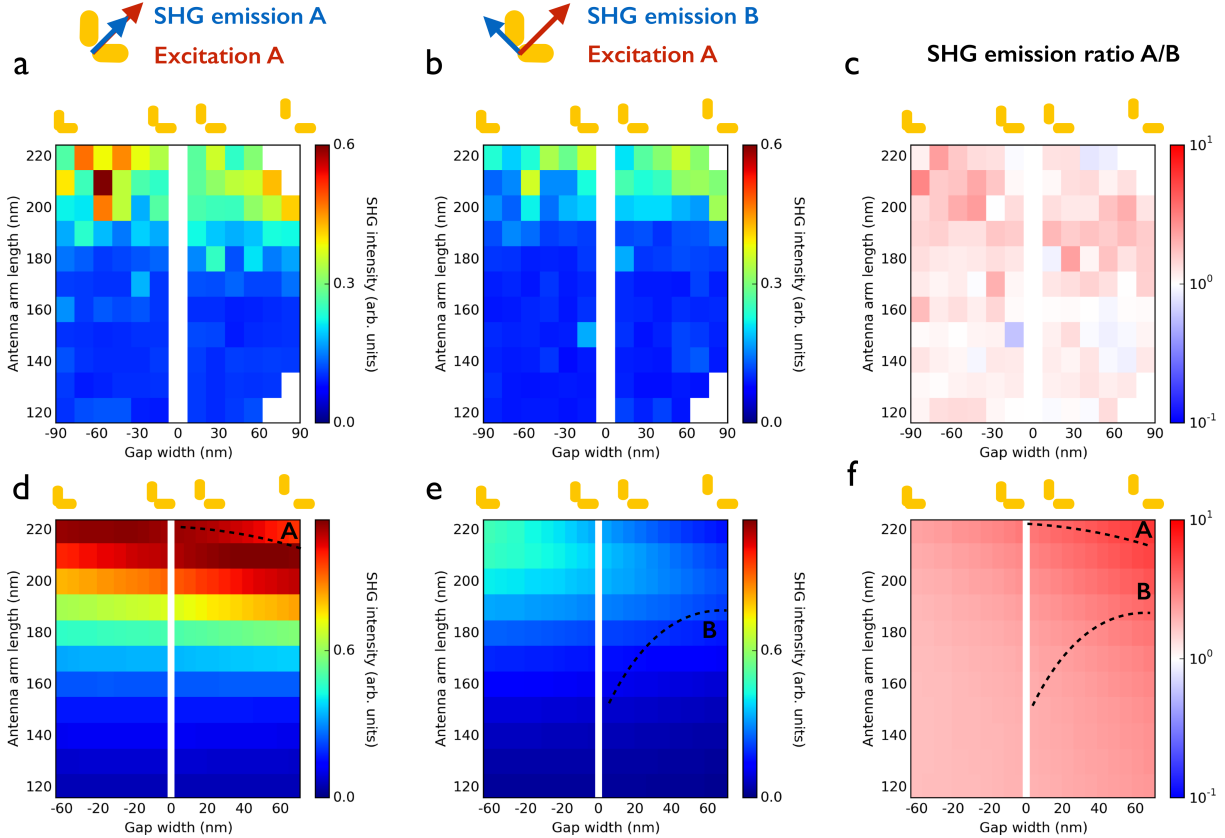
Figure S8: (color online) SHG for an incident E-field at 900 nm and linearly polarized at 45°
(antibonding), for detection polarization along the anti-bonding (A) polarization of 45° (a)
and the bonding (B) polarization of -45° (b). (c) Ratio of SHG emission along A normalized
to emission along B. (d,e) Calculated SHG emission intensities corresponding to a and b,
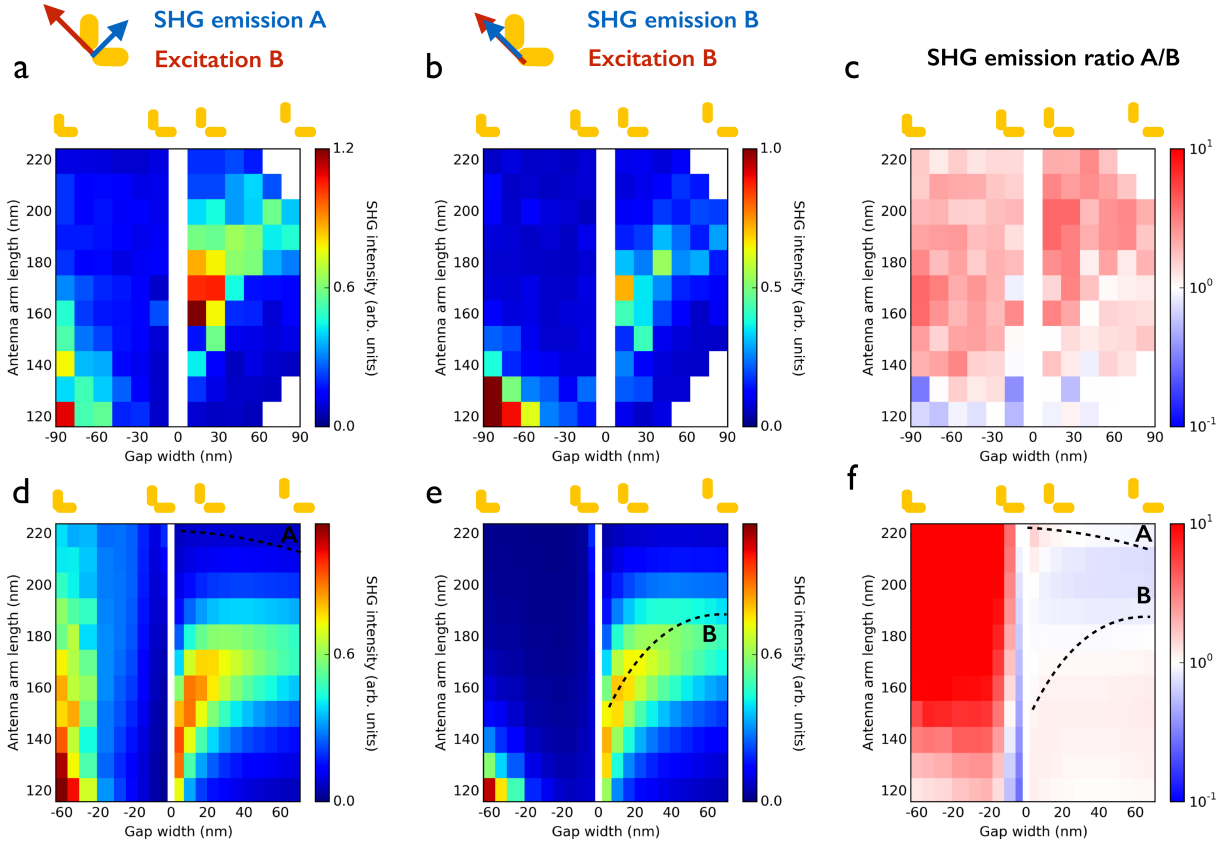with (f) A/B ratio of SHG emission polarization.

Figure S9: (color online) SHG for an incident E-field at 900 nm and linearly polarized at -45° (bonding), for detection polarization along the anti-bonding (A) polarization of 45° (a) and the bonding (B) polarization of -45° (b). (c) Ratio of SHG emission along A normalized to emission along B. (d,e) Calculated SHG emission intensities corresponding to a and b, with (f) A/B ratio of SHG emission polarization.
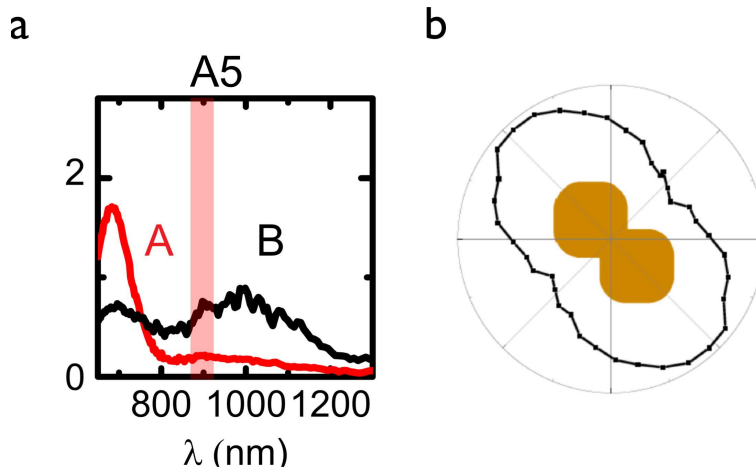

Figure S10: (color online) a) Scattering cross-section measured on antenna A5 (see main text, Figure 1). b) Polarization-resolved SHG intensity for an incident E-field at 900 nm and linearly polarized at -45° (bonding).

10

3 S3 - Microscopic model of Second Harmonic Generation from plasmonic nano-antennas

3.1 Computational method

The microscopic description of Second Harmonic Generation involves three steps: (i) optical excitation of the nano-object by the incident wave, (ii) creation of a non-linear polarization (iii) radiation of the harmonic wave by the non-linear sources. Alternative techniques based on a macroscopic description of the non-linear response based on an effective multipolar tensor have also been proposed for specific experimental configurations.[2,3] Recently, a time-domain implementation of the hydrodynamic model has been recently developed to provide a nonperturbative description of the nonlinear coherent interaction between light and plasmonic nanostructures.[4] Nonlinear metasurfaces can also be described using an extension of the homogenization model to the nonlinear regime.[5]

We have computed the total electric field on the antennas upon optical excitation using a commercial Finite Element Software (COMSOL Multiphysics 4.4b). Special attention has been paid to the symmetry of the computed nanostructures to avoid any artefact and the convergence of the simulations has been carefully verified. Whereas all the results presented in this paper have been obtained from the electric fields calculated using COMSOL, systematic comparison with results obtained using the Green Dyadic Method have been performed to further support our conclusions. Our choice of using COMSOL is mainly justified by the possibility of fast and systematic parameter sweeps. Finite element modelling of nonlinear response in strongly coupled nanostructures is particularly challenging since the precise cancellation of nonlinear dipoles requires either a symmetry in the mesh reflecting the underlying geometrical symmetries, or a very fine meshing to ensure convergence. We have chosen in this work to apply adaptive meshing on the nanoparticle surface with a very small distance between neighbouring nonlinear dipoles in the vicinity of the nano-gap and have achieved consistent results. We do not consider quantum effects, which have been show to play a role

mainly for gaps smaller than 0.5 nm, which is not the case in our work. Also nonlocal effects are not expected to majorly influence the results, as they would only cause some averaging of field fluctuations over neighbouring mesh points.

In a first step, the total electric field at any location on the nanostructure $\mathbf{E}(\mathbf{r}, \omega)$ is computed using the finite element solver assuming a plane wave excitation at normal incidence. The second step of the simulations requires to describe the non-linear sources and relate them to the fundamental electric field on the nanostructure. Gold has bulk inversion symmetry and therefore a zero second order bulk susceptibility in the dipole approximation. However, efficient SHG can be excited in gold nanostructures from two contributions. First, the dipole approximation neglects weaker non-local bulk contributions to the non-linear response such as the ones from magnetic dipoles and electric quadrupoles.[6] Second, the bulk inversion symmetry is broken at the metal surface leading to efficient SHG from gold films or nanostructures.[7] For isotropic and centrosymmetric materials, the second-order surface susceptibility tensor has only three independent components: $\chi_{nnn}^{(2)}$, $\chi_{npp}^{(2)}$ and $\chi_{ppn}^{(2)}$ where n and p denotes perpendicular and parallel components to the surface, respectively. Although there is still a debate on the relative importance of these different components, several studies suggest that the normal component χ_{nnn} yields the largest contribution to the SHG.[7–9] Nevertheless, we have considered all three components and provide in the following the result of systematic simulations of the SHG corresponding to these different nonlinear polarization distributions. We define complex surface non-linear dipoles $\mathbf{p_{NL}}(\mathbf{r}, 2\omega)$ associated to each discretization cell located on the surface of the antenna at position $\mathbf{r}$:

$$\mathbf{p_{NL}}(\mathbf{r}, 2\omega) = \chi^{(2)} : \mathbf{E}(\mathbf{r}, \omega)\, \mathbf{E}(\mathbf{r}, \omega) \tag{1}$$

in which $\chi^{(2)}$ is the non-linear susceptibility and $\mathbf{E}(\mathbf{r}, \omega)$ is the complex amplitude of the total electric field at the surface of the nano-antenna. For the *nnn*, *npp* and *ppn* contributions,

the nonlinear dipoles are respectively written :

$$\mathbf{p_{NL,nnn}}(\mathbf{r}, 2\omega) = \chi_{nnn}^{(2)} E_n(\mathbf{r}, \omega)^2\, \mathbf{e_n}(\mathbf{r})$$

$$\mathbf{p_{NL,npp}}(\mathbf{r}, 2\omega) = \chi_{npp}^{(2)} E_p(\mathbf{r}, \omega)^2\, \mathbf{e_n}(\mathbf{r})$$

$$\mathbf{p_{NL,ppn}}(\mathbf{r}, 2\omega) = \chi_{ppn}^{(2)} E_p(\mathbf{r}, \omega)\, E_n(\mathbf{r}, \omega)\, \mathbf{e_p}(\mathbf{r})$$

in which $E_n(\mathbf{r}, \omega)$ and $E_p(\mathbf{r}, \omega)$ are the normal and parallel to the surface component of the electric field, $\mathbf{e_n}(\mathbf{r})$ and $\mathbf{e_p}(\mathbf{r})$ are normal and parallel to the surface unit vectors. In the computation, we set the nonlinear susceptibility tensor components to 1. The nonlinear sources described by Eq. 2 are complex and therefore the phase information which governs the far-field radiation is taken into account in our calculations.

Then, the SHG electric field radiated by the non-linear dipoles at any location $\mathbf{r}'$ is computed from the asymptotic limit of the field susceptibility of the environment $\mathbf{S_\infty}(\mathbf{r}, \mathbf{r}', 2\omega)$ valid in the far-field at the SHG angular frequency 2ω. The contribution from the substrate is fully accounted for as we include the corresponding field-susceptibility in our calculations:

$$\mathbf{S_\infty}(\mathbf{r}, \mathbf{r}', 2\omega) = \mathbf{S_0}(\mathbf{r}, \mathbf{r}', 2\omega) + \mathbf{S_{surf,\infty}}(\mathbf{r}, \mathbf{r}', 2\omega) \tag{2}$$

The SHG electric field in the far-field can then be written:

$$\mathbf{E_{SHG}}(\mathbf{r}', 2\omega) = \mathbf{S_\infty}(\mathbf{r}, \mathbf{r}', 2\omega).\mathbf{p_{NL}}(\mathbf{r}, 2\omega) \tag{3}$$

To compute the SHG intensity, we integrate the intensity scattered in the solid angle defined by the collecting optics. The numerical aperture of the microscope objective used in our experiments is therefore taken into account in our simulations. For the polarization-resolved plots, we use the same approach but only take into account the electric field with the proper polarization.

3.2 Comparison of the SHG from the $\chi_{nnn}^{(2)}$, $\chi_{npp}^{(2)}$ and $\chi_{ppn}^{(2)}$ nonlinear susceptibility tensor components

In the following, we have systematically computed the SHG intensity from a polarization distribution arising from the $\chi_{nnn}^{(2)}$, $\chi_{npp}^{(2)}$ or $\chi_{ppn}^{(2)}$ components of the nonlinear susceptibility tensor. We compare the computed variations of both the total and polarization-resolved SHG intensity with the experimental results.

We have first focused on the total SHG intensity emitted by a nanoantenna for excitation along either the antibonding or bonding axis as presented in Figure 2 of the main text. Considering only the relative variations or the SHG intensity and SHG excitation ratio with the antenna morphology, Figure S11 already shows that the $\chi_{nnn}^{(2)}$ component provides the best agreement with the experiment. For instance, the SHG intensity predicted by the $\chi_{npp}^{(2)}$ component is not matching the experimental results for neither of the two incident polarizations. The $\chi_{ppn}^{(2)}$ is in better agreement but the intensities calculated for excitation along the bonding axis differ from experiment for long arm antennas. Interestingly, this $\chi_{ppn}^{(2)}$ contribution do not show cancellation in the regime of small gaps. However, the fact that the magnitude of this tensor component is expected to be much smaller that $\chi_{nnn}^{(2)}$,[7–9] the strong variations observed in the SHG polarization and the polarization-resolved intensity maps of Figure S12 are a strong indication that the enhancement of SHG for small gaps is due to local asymmetries in the gap region and not the signature of the *ppn* contribution to SHG.

In Figure 12 and 13, we compare the polarization-resolved SHG intensities generated by the 3 different nonlinear polarization components for excitation along either the antibonding or bonding axis. Here again, the $\chi_{nnn}^{(2)}$ is yielding the best agreement with the experiment. In particular, the SHG detected on connected antennas on the left of the experimental maps of Figure 12 for detection along the antibonding axis are not reproduced by the *ppn* component. From these systematic verifications, we conclude that the normal nonlinear polarization
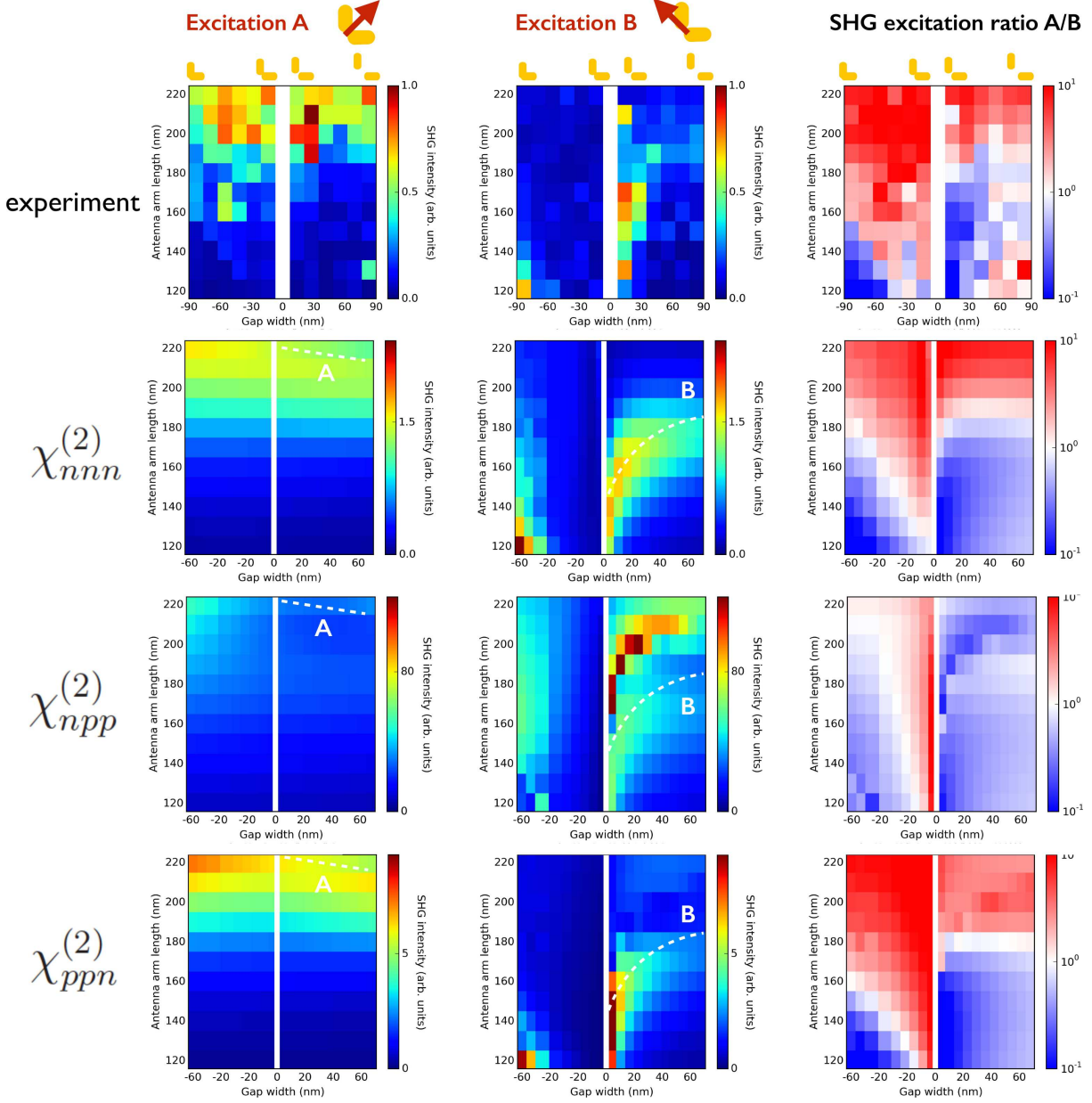
14

Figure S11: (color online) Top row: Total SHG intensity for excitation along antibonding axis (left) or bonding axis (center).Ratio of A/B excitation efficiencies. The following rows present the corresponding quantities computed from different components of the nonlinear susceptibility tensor. Each component was normalized to the maximum of the anti-bonding resonance.

component dominates the response in the investigated antennas. Therefore, in the main text and previous section of the SI, we only present the results of numerical simulations obtained by considering the $\chi^{(2)}_{nnn}$ component of the nonlinear susceptibility tensor. Although, it would
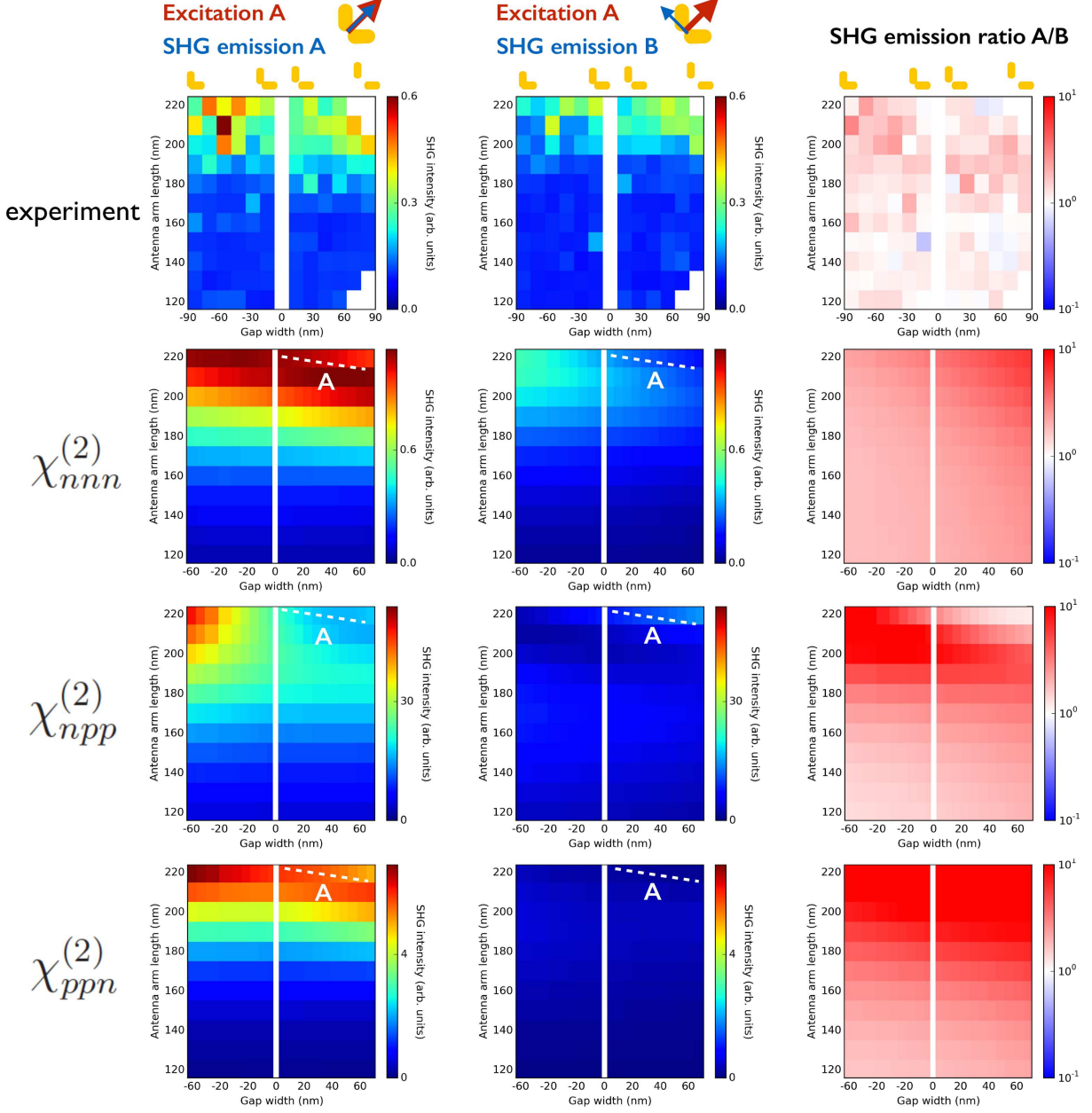
Figure S12: (color online) Top row: SHG intensity for excitation along the antibonding axis and detection polarization along the anti-bonding axis (left) and bonding axis (center). Ratio of SHG emission along A normalized to emission along B. The following rows present the corresponding quantities computed from different components of the nonlinear susceptibility tensor.

in principle be possible to take into account all three contributions in the simulations, too little is known on the relative magnitudes of the NL susceptibility tensor components to avoid arbitrariness.
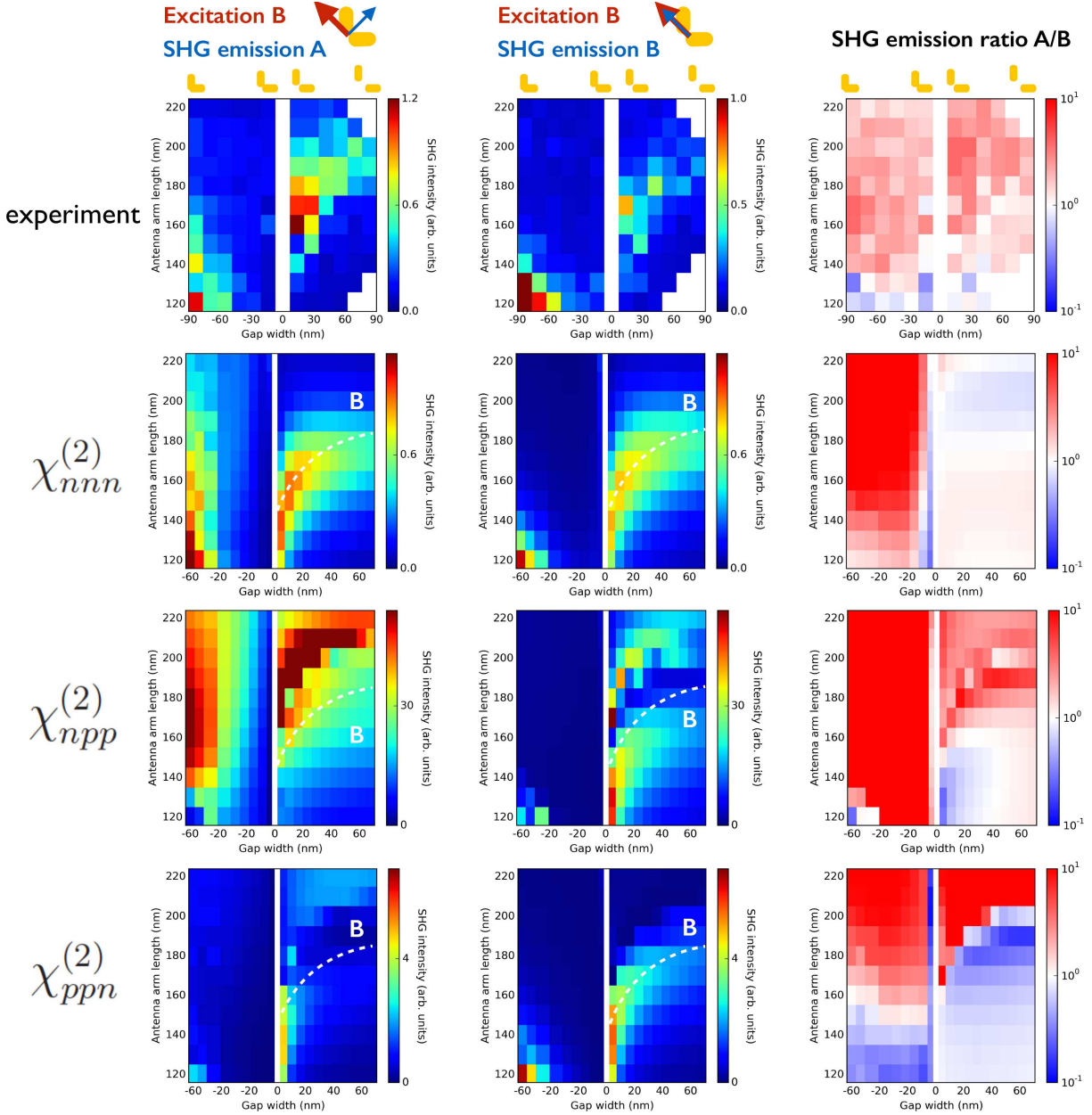
Figure S13: (color online) Top row: SHG intensity for excitation along the bonding axis and detection polarization along the anti-bonding axis (left) and bonding axis (center). Ratio of SHG emission along A normalized to emission along B. The following rows present the corresponding quantities computed from different components of the nonlinear susceptibility tensor.

References

(1) Black, L.-J.; Wang, Y.; de Groot, C. H.; Arbouet, A.; Muskens, O. L. Optimal Polarization Conversion in Coupled Dimer Plasmonic Nanoantennas for Metasurfaces. ACS Nano **2014**, 8, 6390–6399.

(2) Canfield, B. K.; Kujala, S.; Jefimovs, K.; Svirko, Y.; Turunen, J.; Kauranen, M. A Macroscopic Formalism to Describe the Second-Order Nonlinear Optical Response of Nanostructures. J. Opt. A - Pure Appl. Op. **2006**, 8, S278–.

(3) Zdanowicz, M.; Kujala, S.; Husu, H.; Kauranen, M. Effective Medium Multipolar Tensor Analysis of Second-Harmonic Generation from Metal Nanoparticles. New J. Phys. **2011**, 13, 023025–.

(4) Ginzburg, P.; Krasavin, A. V.; Wurtz, G. A.; Zayats, A. V. Nonperturbative Hydrodynamic Model for Multiple Harmonics Generation in Metallic Nanostructures. ACS Photonics **2015**, 2, 8–13.

(5) Chen, P.-Y.; Alù, A. Subwavelength Imaging Using Phase-Conjugating Nonlinear Nanoantenna Arrays. Nano Lett. **2011**, 11, 5514–5518.

(6) Butet, J.; Bachelier, G.; Russier-Antoine, I.; Jonin, C.; Benichou, E.; Brevet, P.-F. Interference between Selected Dipoles and Octupoles in the Optical Second-Harmonic Generation from Spherical Gold Nanoparticles. Phys. Rev. Lett. **2010**, 105, 077401–.

(7) Wang, F.; Rodriguez, F.; Albers, W.; Ahorinta, R.; Sipe, J.; Kauranen, M. Surface and Bulk Contributions to the Second-Order Nonlinear Optical Response of a Gold Film. Phys. Rev. B **2009**, 80, 233402.

(8) Bachelier, G.; Butet, J.; Russier-Antoine, I.; Jonin, C.; Benichou, E.; Brevet, P.-F. Origin of Optical Second-Harmonic Generation in Spherical Gold Nanoparticles: Local Surface and Nonlocal Bulk Contributions. Phys. Rev. B **2010**, 82, 235403–.

(9) Mikitalo, J.; Suuriniemi, S.; Kauranen, M. Boundary Element Method for Surface Non-linear Optics of Nanoparticles. <u>Opt. Express</u> **2011**, <u>19</u>, 23386–23399.